

# Spherical symmetry breaking in cold gravitational collapse of isolated systems

Tirawut Worrakitpoonpon<sup>1\*</sup>

<sup>1</sup>*Division of Physics, Faculty of Science and Technology, Rajamangala University of Technology Suvarnabhumi, Nonthaburi Campus, 7/1 Nonthaburi 1 Road, Nonthaburi 11000, Thailand*

21 November 2014

## ABSTRACT

We study, using  $N$ -body simulation, the shape evolution in gravitational collapse of cold uniform spherical system. The central interest is on how the deviation from spherical symmetry depends on particle number  $N$ . By revisit of the spherical collapse model, we hypothesize that the departure from spherical symmetry is regulated by the finite- $N$  density fluctuation. Following this assumption, the estimate of the flattening of relaxed structures is derived to be  $N^{-1/3}$ . In numerical part, we find that the virialized states can be characterized by the core-halo structures and the flattenings of the cores fit reasonably well with the prediction. Moreover the results from large  $N$  systems suggest the divergence of relaxation time to the final shapes with  $N$ . We also find that the intrinsic shapes of the cores are considerably diverse as they vary from nearly spherical, prolate, oblate or completely triaxial in each realization. When  $N$  increases, this variation is suppressed as the final shapes do not differ much from initial symmetry. In addition, we observe the stable rotation of the virialized states. Further investigation reveals that the origin of this rotation is related in some way to the initial density fluctuation.

**Key words:** gravitation-methods: numerical-galaxies: elliptical and lenticular, cD-galaxies: formation.

## 1 INTRODUCTION

Elliptical galaxies have been known for a long time and constituted one of the main categories of modern galaxy classification. Observationally it is clear that they are in some form of virialized states with surface brightness suiting the well-known de Vaucouleurs profile (de Vaucouleurs 1953). In attempt to answer this, D. Lynden-Bell introduced the violent relaxation theory (see Lynden-Bell 1967) which regarded the observed galaxies as meta-stable equilibria resulting from the collisionless relaxation. This evolution time-scale was notably short so that the protogalaxies were able to attain the stationary states within a few crossing times. Although the theory of Lynden-Bell was considered to be a milestone for understanding the collisionless dynamics of self-gravitating systems and, more generally, the systems governed by other long-range interactions, it did not provide a satisfactory explanation of how the elliptical galaxies had obtained their shapes. As a consequence the question about the evolutionary background to those observed ellipticities then became the open research topic in galactic astrophysics and cosmology.

Current understanding suggests two distinctive formation schemes: merger of galaxies and violently collapsing protogalaxy. The former scenario has been suggested by Toomre & Toomre (1972); Toomre (1977) which involved at least two encountering galaxies under mutual gravitational interaction. It was shown that the final shape after the merger could be elliptical. Numerous merging simulations producing galaxies similar to those from observations were reported (see, for example, Barnes & Hernquist 1996 and references therein). In the latter scenario, people were focusing on the isolated radially anisotropic system under the gravitational force. It was long believed that such a system is highly unstable to the deformation of configuration. The instability was first detected in the pioneering simulation by Hénon (1973), who figured out that under a circumstance where system was dominated by radial motion, the spatial configuration of system was drastically deformed. Similar result was obtained later by Polyachenko (1981) in which, starting from the predominantly radial spherical system, an ellipsoidal core of structure was observed. These results gave rise to the so-called radial orbit instability (ROI), which was originally mentioned by Antonov (1973) (see summary in English in de Zeeuw 1987). For the isotropic system it was known that any distribution function was always sta-

\* E-mail: worraki@gmail.com

ble as long as it was the decreasing function of energy per unit mass (see Antonov 1961; Doremus et al. 1971).

Although the ROI theory did not provide any clue on precise stability rule, many subsequent studies were able to determine, semi-analytically or numerically, the criteria at which shape deformation was triggered. Various diagnostics were then proposed. Studies led by Merritt & Aguilar (1985); Palmer & Palaloizou (1987); Barnes et al. (1986) showed that an anisotropic ratio calculated from twice the radial kinetic energy over the tangential kinetic energy was sufficient to evaluate the stability. Each group finished up with different numerical threshold values but they all shared the same conception that large anisotropic ratio increased the chance of shape deformation. On the other hand, groups of Min & Choi (1989); Cannizzo & Hollister (1992); Theis & Spurzem (1999) used an indicator as simple as the initial virial ratio. In the case of sufficiently low initial virial ratio, it was found that the violently collapsing phase occurred, which was analogous to the radially anisotropic system, and the final shape was considerably changed. Later there was also the report of study using the combination of both parameters (see Barnes et al. 2009). In another aspect, it was proposed that the instability could be engendered by density contrast from the inhomogeneity of initial density profile (see Roy & Perez 2004). Later the same instability in dissipative systems was also examined by Maréchal & Perez (2010).

Question on intrinsic three-dimensional shape of elliptical galaxies is still unsolved. It was long believed that elliptical galaxy is oblate due to the flattening about the axis of rotation. Theoretical supports for oblate galaxy could be found in Dehnen & Gerhard (1994); Robijn & de Zeeuw (1996) and also references therein. An objection was then made based on the observed rotational velocity of galaxies that led to another propositions for prolate galaxy (e.g. Binney 1978) and triaxial galaxy (e.g. Schwarzschild 1979, 1982; de Zeeuw 1985). Numerical works of cold collapse experiments starting from various density profiles (see Aguilar & Merritt 1990; Cannizzo & Hollister 1992; Boily & Athanassoula 2006 for example) also produced different results. They found that the final intrinsic shapes were not unique but they depended strongly on the choices of initial conditions. However, the investigation on this topic relies mainly on theoretical and numerical approaches due to the observational limitation.

In this paper we investigate the shape evolution in the cold collapse of isolated self-gravitating system in spherical symmetry. We are interested in the aspects different from those in the past literatures: what is the role of finite- $N$  density fluctuation in the evolution from spherical symmetry and how can we describe, in the quantitative way, its influence on the final shapes. This paper is organized as follows. First in Section 2, we revisit the dynamical model of cold gravitational collapse of spherical system and derive the estimate of some variables in stationary states as a function of  $N$  such as the flattening and specific angular momentum. These predictions will be used in comparing with numerical results in further section. In Section 3, we introduce the initial condition and simulation parameters that we employ in this work. Next in Section 4, we present the numerical results, focusing mainly on the temporal evolution of systems and their properties in stationary states. Some of the results may be compared with theoretical predictions we de-

rived earlier. Finally in Section 5, we give the conclusion and discussion.

## 2 DYNAMICS OF COLD GRAVITATIONAL COLLAPSE

This section describes in detail our theoretical study of spherical cold collapse. We first recall the dynamical model of this process in continuum limit. Then, we apply the density fluctuation and derive the estimate of some variables in stationary states as a function of  $N$ . Results from this section will be used in comparing with numerical results in Section 4.

### 2.1 Shape evolution in system with finite $N$

Consider a spherically symmetric system in continuum limit with uniform density  $\rho_0$ ; the equation of motion of a thin spherical mass shell with radial position  $r$  at time  $t$  is given by

$$\frac{\partial^2 r}{\partial t^2} = -\frac{GM_r}{r^2} \quad (1)$$

where  $M_r = 4\pi \int_0^r \rho_0 r'^2 dr'$  is the total mass inside  $r$ . Defining the scale factor  $R = r/r_0$ , the equation of motion can be rewritten in terms of  $R$  as

$$\frac{\partial^2 R}{\partial t^2} = -\frac{GM_r}{r_0^3 R^2}. \quad (2)$$

For cold initial state, the integration of equation (2) over  $t$  gives

$$\frac{\partial R}{\partial t} = -\left[\frac{2GM_r}{r_0^3} \frac{(1-R)}{R}\right]^{1/2}, \quad (3)$$

which describes the infall velocity before the maximum collapse, i.e. when  $R = 0$ . The solution of equation (3) can be written in parametric form as follows:

$$R = \cos^2 \beta \quad (4)$$

$$t = \left(\frac{r_0^3}{2GM_r}\right)^{1/2} \left[\beta + \frac{\sin 2\beta}{2}\right]. \quad (5)$$

For the uniform case, all mass shells will collapse simultaneously into a singularity at the free-fall time,  $t_{ff}$ , given by

$$t_{ff} = \sqrt{\frac{3\pi}{32G\rho_0}}. \quad (6)$$

Consider now a system of  $N$  particles; the local density fluctuation arising from finite  $N$  makes the free-fall time of each particle scattered around the mean value (6). Consequently, the dispersion of free-fall time can be written by

$$\delta t_{ff} = -\frac{1}{2} \left(\frac{\delta \rho_0}{\rho_0}\right) t_{ff} \quad (7)$$

where  $\delta \rho_0$  is the density fluctuation. Then, it can be shown that the dispersion of infall velocity at any  $t$  can be approximated by

$$\delta \dot{R} \sim \frac{\delta t_{ff}}{t_{ff}} \times \frac{\partial R}{\partial t}. \quad (8)$$

The variation of  $\delta \dot{R}$  means that the particles having shorter

free-fall times will have greater infall velocities. This implies that with microscopic density fluctuation the gravitational collapse is no longer in perfect singularity at  $t_{ff}$ . The minimal size,  $R_{min}$ , is instead attained which can be scaled with  $N$  as, following the analysis of Boily et al. (2002),

$$R_{min} \propto N^{-1/3}. \quad (9)$$

Further from that the finite- $N$  effect prevents the collapse to attain the absolute singularity, the velocity dispersion (8) also becomes the source of the departure from spherical symmetry in the following manner. Given the particles falling to the origin from all directions with velocity dispersion in equation (8), they will be moving outwards with different velocities. We speculate that during the process of shape evolution the particles with greater outward velocities tend to expand further and then they are more likely to establish the longer axis. Before we start the estimation, we first suppose that, when the violent relaxation is finished after the cold collapse, the final shape of bound structure is always in ellipsoidal form having three calculable semi-principal axes of lengths  $a, b$  and  $c$  such that  $a \geq b \geq c$ . To evaluate the degree of departure from spherical symmetry, we define the flattening  $\iota$  as

$$\iota = \frac{a - c}{a}. \quad (10)$$

By definition  $\iota$  ranges from 0 (sphere) to 1 (thin disc). As it was noticed by Casertano & Hut (1985) that the determination of system size is significantly sensitive to the choice of the positioning of coordinate frame, we then impose that the calculations of all physical quantities of the stationary structures are fixed on the centre of gravity coordinate. This is also in correspondence with analysis of numerical results in Section 4.

To estimate the flattening of the final shape, let us suppose that the permitted relaxation time to the final shape is given by  $t_{relax}$ . We then estimate the semi-major axis length by the distance spanned by a particle with maximum outward velocity, i.e.

$$a \sim \dot{R}_{max} t_{relax} \quad (11)$$

where  $\dot{R}_{max}$  is the maximum infall velocity. For the same reason, the semi-minor axis length corresponds to

$$c \sim (\dot{R}_{max} - \dot{R}) t_{relax}. \quad (12)$$

The expressions above imply that the key development to triaxiality relies on the dispersion of infall velocity passing at the origin at  $t_{ff}$ . Then, we approximate the maximum velocity by

$$\dot{R}_{max} \sim \frac{R(0)}{t_{ff} - \delta t_{ff}}, \quad (13)$$

where  $R(0)$  is the initial position. If we suppose that  $\delta t_{ff} \ll t_{ff}$ , we therefore obtain the estimate of  $\iota$  of the stationary states to be

$$\iota \propto \langle \delta \dot{R} \rangle_{t=t_{ff}} \propto \frac{\langle \delta t_{ff} \rangle}{t_{ff}} \left[ \frac{\partial R}{\partial t} \right]_{t=t_{ff}}, \quad (14)$$

where  $\langle \rangle$  denotes the average. To explain the approximation (14) in other words, the origin of flattening comes from the combination of two main factors which are the dispersion of  $t_{ff}$  and the mean infall velocity at  $t_{ff}$ . Replacing the

relations (3) and (7) into (14) and taking  $R_{min} \ll 1$ , the estimate becomes

$$\iota \propto \left\langle \frac{\delta \rho_0}{\rho_0} \right\rangle \frac{1}{R_{min}^{1/2}}. \quad (15)$$

In the case of uniform density discretized into point-mass system of randomly placed  $N$  particles, the average density fluctuation can be approximated by Poissonian noise, i.e.  $\langle \delta \rho_0 / \rho_0 \rangle \sim 1/\sqrt{N}$ . Following the scaling of  $R_{min}$  given by equation (9), the estimate of  $\iota$  becomes

$$\iota \propto N^{-1/3}. \quad (16)$$

The scaling (16) implies that the stationary state is less deformed as  $N$  increases since the density fluctuation triggering the shape evolution is diminished. Note that the advantage of choosing the uniform case is that the density fluctuation is purely that of Poisson, which is essentially a function of only  $N$ . Therefore, the estimated flattening of stationary states can be characterized just by a single parameter. Analysis of non-uniform initial condition is more complicated as the density fluctuation does not only come from Poissonian noise. So the prediction might involve more than one parameter.

In general, the violent relaxation of cold initial state is always followed by the process of mass ejection that expels an amount of mass away from the system (see, e.g., McGlynn 1984; Aarseth et al. 1988; Joyce et al. 2009; Sylos Labini 2012, 2013). Therefore, the mass of the virialized state is always reduced from that of initial state. In our analysis, we neglect all ejected particles and only the remaining bound part is in consideration.

## 2.2 Generation of angular momentum

We investigate further the generation of angular momentum from cold collapse. Given the local density fluctuation, the trajectories of infall particles are meant to deviate from completely radial. Thus, at  $t_{ff}$  when the particles pass by the origin, they can gain some rotational component. In cold non-rotating initial state, we speculate that the angular momentum of relaxed structure is produced by the exchange between the escaping particles and the remaining bound particles during the violent relaxation. The mass ejection is supposed to be asymmetric so that the exchanged angular momentum is not cancelled out.

From equation (3), we can deduce that at  $t_{ff}$  the infall velocity diverges in continuum limit. But if  $N$  is finite, the same discreteness that prevents the singularity also imposes the limit of the infall velocity. We estimate the average infall velocity that can be attained at  $t_{ff}$  by taking the limit  $R \rightarrow R_{min}$  where  $R_{min} \ll 1$  and we therefore have

$$v_{ff} = \sqrt{\frac{GM}{R_{min}}} \propto N^{1/6}. \quad (17)$$

Note that this expression is in line with Joyce et al. (2009). Suppose that the perpendicular distance to the origin of particles is given by  $R_{min}$ , the estimate of accumulated angular momentum of a system composed of  $N_b$  bound particles of mass  $m$  therefore reads

$$L \propto m N_b v_{ff} R_{min}. \quad (18)$$

To avoid the complexity arising from  $N$ -dependence of  $N_b$ ,

it is more convenient to consider the specific angular momentum  $j = L/mN_b$ . We therefore obtain the scaling of  $j$  as a function of  $N$  following the relations (9) and (17) as

$$j \propto v_{ff} R_{min} \propto N^{-1/6}. \quad (19)$$

This means that the net rotational motion vanishes in the continuum limit since the evolution is completely radial at all time.

### 3 N-BODY SIMULATION SETUP

#### 3.1 Initial condition and units

In this study, the initial condition is the sphere of uniform density composed of  $N$  particles of identical mass where all particles are at rest (i.e. cold uniform sphere). To generate it for any  $N$ , particles are thrown randomly in a sphere of radius  $r_0$  with uniform probability density, i.e.

$$P(\vec{r}) = \begin{cases} 1/(\frac{4}{3}\pi r_0^3) & ; \quad |\vec{r}| \leq r_0 \\ 0 & ; \quad \text{elsewhere.} \end{cases} \quad (20)$$

The total mass  $M$  is fixed to  $\frac{4}{3}\pi r_0^3$ ; thus, the mass of individual particle  $m$  is equal to  $\frac{4}{3}\pi r_0^3/N$ . Note that by this choice of parameters, the initial density  $\rho_0$  is always equal to 1. The initial potential energy of a sphere is thus

$$U_0 = -\frac{3GM^2}{5r_0}. \quad (21)$$

Here we put  $r_0 = 0.5$  for all simulations. For temporal evolution, the time unit is presented in the free-fall time given by

$$t_{dyn} = \sqrt{\frac{3\pi}{32G\rho_0}}. \quad (22)$$

In statistical point of view, with  $G$ ,  $M$  and  $r_0$  fixed, it remains only the random microscopic density fluctuation to vary in each realization with mean density contrast decaying with  $N$ . To put it simply, if we fix those three parameters, there is only a single parameter that characterizes the initial condition. For convenience we choose it to be  $N$ . This choice is proper when comparing with the theoretical predictions as we derive them in terms of  $N$ .

#### 3.2 Simulation parameters

Equation of motion of each particle is integrated using GADGET-2 code in public version (see Springel et al. 2001; Springel 2005 for guidance). We consider purely self-gravitating system in non-expanding background. The gravitational force is softened by a spline with adjustable softening length  $\varepsilon$  in the way that it converges to Newtonian above  $\varepsilon$ , but below that length the force is decreasing and vanishes as distance goes to zero (see Springel et al. 2001 for detail). Given an initial system size of order 1, the average inter-particle distance  $\ell$  can be approximated by  $\ell \approx 1/N^{1/3}$ . We then adjust the softening length as decreasing function of  $N$  as

$$\varepsilon = 0.028\ell = \frac{0.028}{N^{1/3}}. \quad (23)$$

We choose  $\varepsilon$  much smaller than  $\ell$  to ensure that the Newtonian gravity is well preserved in close encounters during the

collapse. Although it was found by Boily & Athanassoula (2006) that varying  $\varepsilon$  has significant change on the final shapes, our choice of  $\varepsilon$  is well below the range where the final shapes are sensitive to it. We can hereby neglect the dependence on  $\varepsilon$  in our study.

In dynamical integration, the total force on an individual particle is determined by direct summation at each time step. We separate the simulation into three phases: pre-collapse ( $0 - 0.5 t_{dyn}$ ), collapse ( $0.5 - 1.5 t_{dyn}$ ) and post-collapse (after  $1.5 t_{dyn}$ ). During each phase, the integration time step is fixed. The time steps for pre-collapse and collapse, where the maximum contraction occurs, are controlled to be around  $t_{dyn}/2000$  and  $t_{dyn}/20000$ , respectively. In post-collapse, it varies from  $t_{dyn}/5000$  to  $t_{dyn}/10000$  so that, in all realizations, the error on total energy is less than 0.2% for  $N < 10000$  and 0.5% for  $N > 10000$  at the end of simulations.

## 4 NUMERICAL RESULTS

The numerical simulations are performed for  $N = 1000, 2000, 4000, 8000, 16000$  and  $32000$  with 70, 40, 30, 30, 6 and 2 different realizations, respectively. All simulations are terminated at  $t = 14.28 t_{dyn}$  at first, with prolongation to  $28.56 t_{dyn}$  for a few selected cases with  $N = 16000$  and  $32000$  for specific inquiry. Here, the system of  $N$  which is not too large is preferred in order to preserve the statistical effect from density fluctuation that diminishes substantially with  $N$ . We overcome the anticipated uncertainty arising in small  $N$  system by the ensemble average over considerable number of realizations if necessary.

#### 4.1 Temporal evolution of $\iota$

We consider first the temporal evolutions of shapes of the bound structures. In correspondence with the theoretical framework, the stationary states formed by bound particles are assumed to be ellipsoidal. To determine the semi-principal axis lengths in the course of evolution, we calculate first the moment of inertia tensor at any time  $t$

$$I(t) = \begin{bmatrix} I_{x'x'}(t) & I_{x'y'}(t) & I_{x'z'}(t) \\ I_{y'x'}(t) & I_{y'y'}(t) & I_{y'z'}(t) \\ I_{z'x'}(t) & I_{z'y'}(t) & I_{z'z'}(t) \end{bmatrix} \quad (24)$$

where each element is determined in the centre of mass coordinate of the bound system. The moments of inertia about three principal axes, i.e.  $I_{xx}$ ,  $I_{yy}$  and  $I_{zz}$ , correspond to the eigenvalues of the matrix (24). We arrange them such that  $I_{xx} \leq I_{yy} \leq I_{zz}$  and then the lengths of semi-principal axes associated with  $I_{xx}$ ,  $I_{yy}$  and  $I_{zz}$  are, respectively,

$$\begin{aligned} a &= \sqrt{\frac{5}{2mN_b}(I_{yy} + I_{zz} - I_{xx})} \\ b &= \sqrt{\frac{5}{2mN_b}(I_{zz} + I_{xx} - I_{yy})} \\ c &= \sqrt{\frac{5}{2mN_b}(I_{xx} + I_{yy} - I_{zz})}. \end{aligned} \quad (25)$$

By our manipulation we then have  $a \geq b \geq c$ . The eigenvectors corresponding to those three principal axes, i.e.  $\hat{e}_{xx}$ ,  $\hat{e}_{yy}$  and  $\hat{e}_{zz}$ , are also calculated for further purpose.



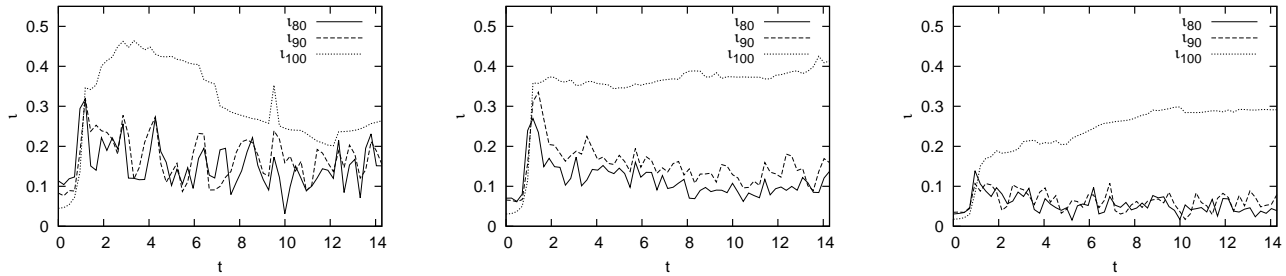


**Figure 1.** Temporal evolutions of  $\iota_{80}$ ,  $\iota_{90}$  and  $\iota_{100}$  for selected realizations with  $N = 1000$  (left),  $4000$  (middle) and  $8000$  (right). Time unit is presented in dynamical time.

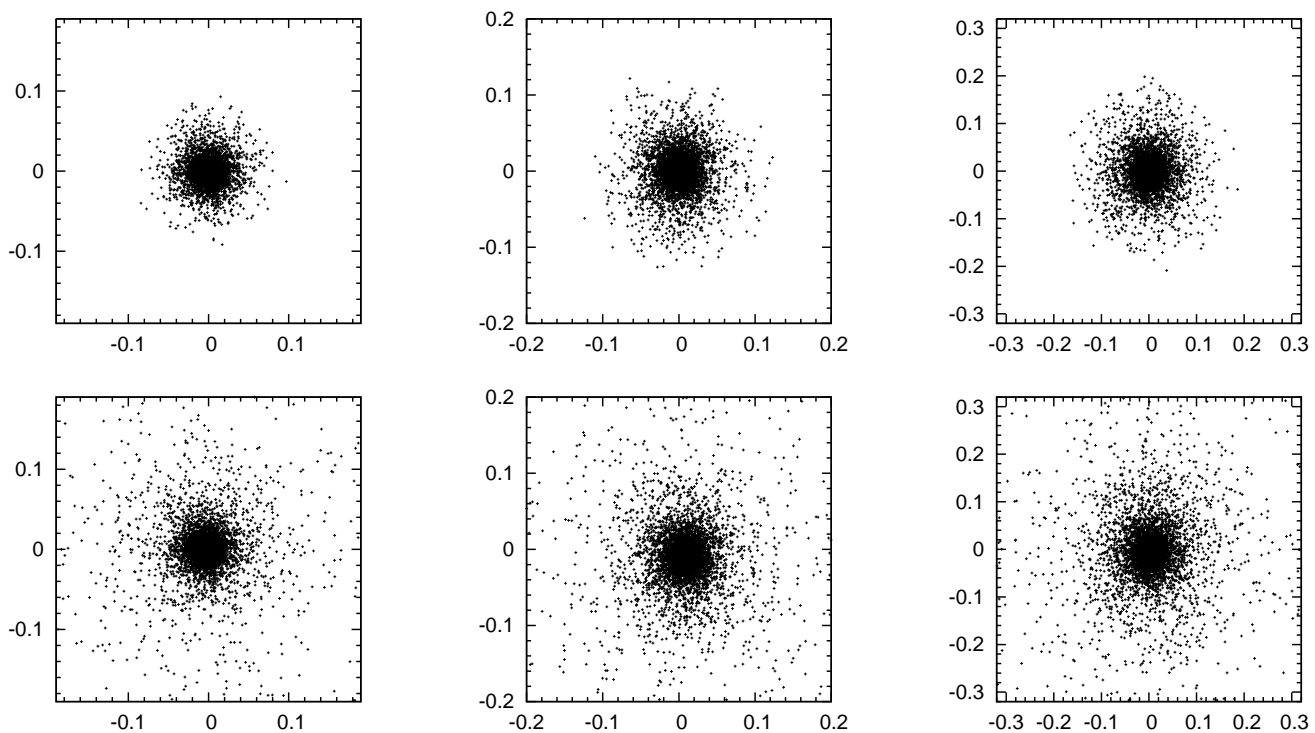


**Figure 2.** Configurations of three selected systems with  $N = 8000$  at the end of simulations. Two left-hand panels correspond to the case in Fig. 1 (right) with  $\iota_{80} = 0.039$ . Two middle panels and two right-hand panels show two cases with  $\iota_{80} = 0.132$  and  $0.142$ , respectively, which are the two most flattened cases. Three top panels indicate distributions of 80% most bound mass projected on to their  $(\hat{e}_{zz}, \hat{e}_{xx})$  planes while three bottom panels correspond to distributions of 100% bound mass projected on to the same planes of their 80% bound structures. Length unit is defined in Section 3.1.

Here, we consider  $\iota$  of three different fractions of mass which are 80%, 90% most bound mass and 100% bound mass, hereby  $\iota_{80}$ ,  $\iota_{90}$  and  $\iota_{100}$ , respectively. Shown in Fig. 1 are temporal evolutions of  $\iota_{80}$ ,  $\iota_{90}$  and  $\iota_{100}$  for selected realizations with  $N = 1000, 4000$  and  $8000$ . Consider first  $\iota_{80}$  and  $\iota_{90}$ ; they increase and settle down to the stationary states giving non-zero flattenings within a few oscillations. This stage corresponds to the collisionless (or mean-field) relaxation as demonstrated, using the same type of initial condition, by Joyce et al. (2009). It was shown by them that the virialization was fully achieved by this process. The evolutionary paths of both parameters are qualitatively similar. The fluctuation of the stationary state is observed, which is more smoothed out as  $N$  increases. This persistence of oscillations with period about the dynamical time may corre-

spond to the remnant of the parametric resonance, originally studied by Levin et al. (2008), which is specific for the violent relaxation of cold initial condition and is responsible for the mass and energy ejection. In contrast,  $\iota_{100}$  evolves differently as it separates from  $\iota_{80}$  and  $\iota_{90}$  since the first dynamical time. Its evolution is moreover unpredictable as, after the cold collapse, it can increase, decrease or remain unchanged before reaching the stationary value. The relaxation times of  $\iota_{100}$  vary considerably from realization to realization. The flattening estimated from  $\iota_{100}$  is higher than using  $\iota_{80}$  and  $\iota_{90}$  but the fluctuation is more smoothed out and the amplitude is apparently uncorrelated to  $N$ .

We investigate further the spatial configurations of the stationary states. Shown in Figs. 2 are the distributions of 80 and 100 per cent bound mass for three selected cases with

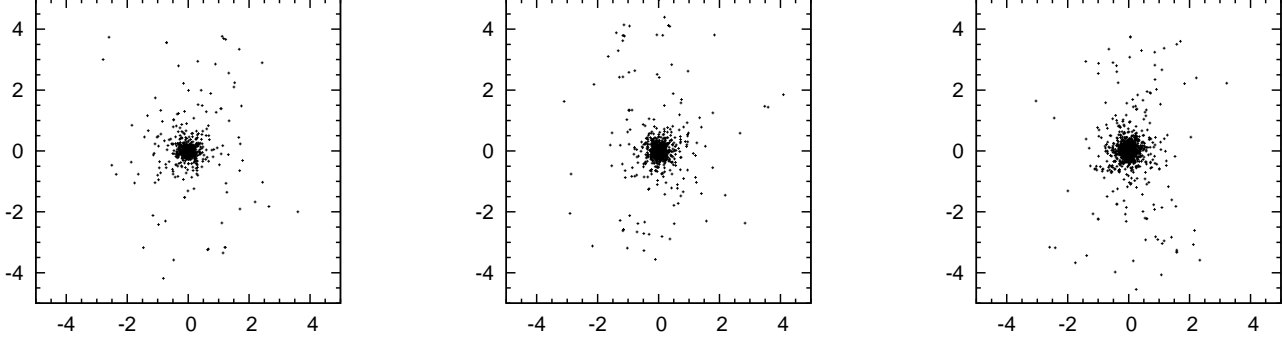


**Figure 3.** Distributions of 100% bound mass projected on to their  $(\hat{e}_{zz}, \hat{e}_{xx})$  planes for the same three cases presented in Figs. 2 in the enlarged coordinate frame.

$N = 8000$  at  $t = 14.28 t_{dyn}$ . One of them corresponds to the case in the right-hand panel of Fig. 1, with  $\iota_{80} = 0.039$ , and two others are with  $\iota_{80} = 0.143$  and  $0.123$ , representing the two most flattened realizations for this  $N$ . In each case, both snapshots are projected on to the  $(\hat{e}_{zz}, \hat{e}_{xx})$  plane of the 80 per cent bound mass, i.e. the plane where we see the structure of 80 per cent bound mass most elongated in the vertical axis, with use of the eigenvectors determined beforehand. Considering first of all the configurations of 100 per cent bound mass, we find that these structures are constituted from the central dense region with surrounding particles in the outer diluted region. This kind of structure can be identified as the ‘core-halo’ that was discovered in many previous works. When comparing these two fractions of mass, we find that the central regions of 100 per cent bound structures are similar to the 80 per cent bound structures while the difference between those two is more remarked in the surrounding region. So, it is reasonable to say that the 80 per cent bound mass represents the core of the stationary state. Now let us examine the configurations of the cores. We observe in all three cases the elliptical cores with various sizes and flattenings in line with the reported  $\iota_{80}$ .

To investigate more in detail the 100 per cent bound structures, the distributions of 100 per cent bound mass for the same cases in Fig. 2 are plotted in Fig. 3, now in enlarged coordinate frames and projected on to their own  $(\hat{e}_{zz}, \hat{e}_{xx})$  planes. In these figures, we find distant particles far from the core and most of them are situated near the major principal axis. However, it is clear that the projected configurations when including those outermost particles in the halo are not elliptical. This explains why the flattening estimated from  $\iota_{100}$  is higher than using  $\iota_{80}$  or  $\iota_{90}$  since those particles, albeit a few, are dominant in calculating  $\iota_{100}$ . It therefore turns out to be that the parameter  $\iota_{100}$  can attain the stationarity even though the entire configuration is not necessarily ellipsoidal.

These results suggest that  $\iota_{80}$  is appropriate for studying the intrinsic shapes of stationary states but, in contrast,  $\iota_{100}$  is found to be inaccurate. We also find no significant difference between using  $\iota_{80}$  and  $\iota_{90}$ .

#### 4.2 $N$ -dependence of $\iota$

In this section, we examine the  $N$ -dependence of the flattening of the stationary states. First, the log-log plot of ensemble-averaged  $\iota_{80}$  from simulations as a function of  $N$

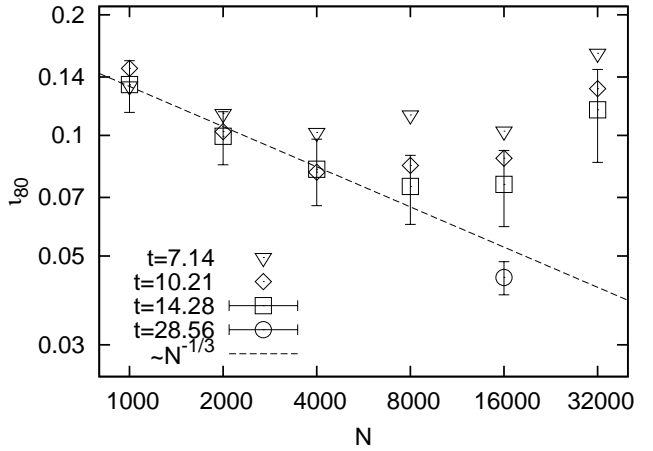


**Figure 4.** Log-log plot of ensemble-averaged  $\iota_{80}$  as a function of  $N$  measured at  $t = 7.14, 10.21$  and  $14.28 t_{dyn}$ , with a few cases extended to  $28.56 t_{dyn}$ . Dashed line corresponds to the  $N^{1/3}$  best fit following equation (16) with data from  $N < 10000$  at  $t = 14.28 t_{dyn}$ . Widths of error bars are estimated from standard deviation over realizations, except for  $N = 32000$  where it corresponds to the difference between two realizations.

at different time slices after virialization is shown in Fig. 4. To obtain each point, the flattening is determined individually in each realization before being averaged. Straight line corresponds to the  $N^{-1/3}$  best fit following equation (16) with points from  $N \leq 8000$  at  $t = 14.28 t_{dyn}$ . Error bars at  $t = 14.28 t_{dyn}$  correspond to the standard deviation calculated over realizations, except for  $N = 32000$  where the width corresponds to the difference between two realizations. Let us consider first the evolution of first three time slices. We see that the prediction fits well with simulated results from  $N = 1000, 2000$  and  $4000$  at  $t = 14.28 t_{dyn}$ . At  $7.14 t_{dyn}$ , it appears that the points from two latter cases are not completely relaxed, which might indicate another evolution stage that reshapes the virialized core to the prediction. This evolution is seen more clearly in the  $N = 8000$  case in which at  $t = 7.14 t_{dyn}$  the measured  $\iota_{80}$  is above the  $N^{-1/3}$  line while, as time progresses, it is approaching down to the prediction. At  $t = 14.28 t_{dyn}$ , the point is acceptably close to the prediction. We also notice this evolution for  $N = 16000$  and  $32000$  but the simulations cannot attain the predicted

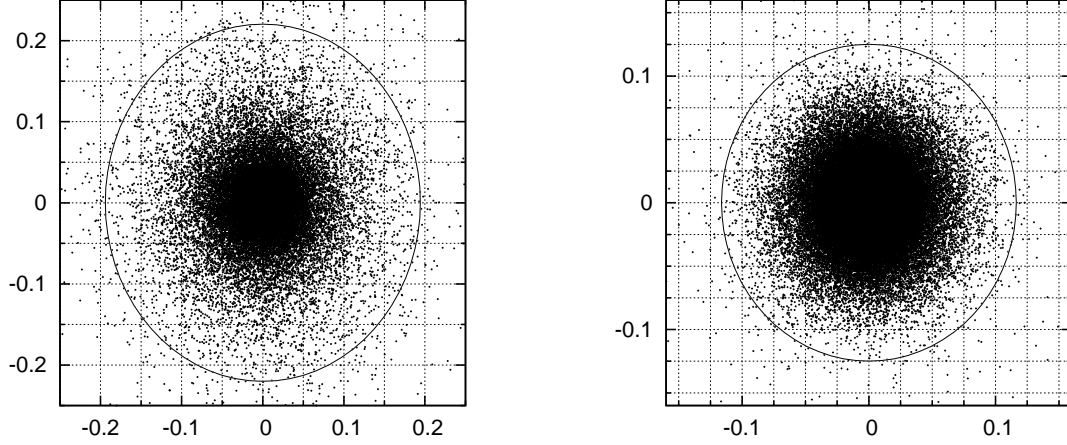


**Figure 5.** Superpositions of  $(\hat{e}_{zz}, \hat{e}_{xx})$  projections of 80% bound particles from all realizations with  $N = 1000$  (left) and  $N = 8000$  (right) at  $t = 14.28 t_{dyn}$ . The ensemble-averaged  $\iota_{80}$  are equal to 0.13 and 0.075, respectively. Ellipses in solid lines correspond to the  $\iota_{80}$  at that time.

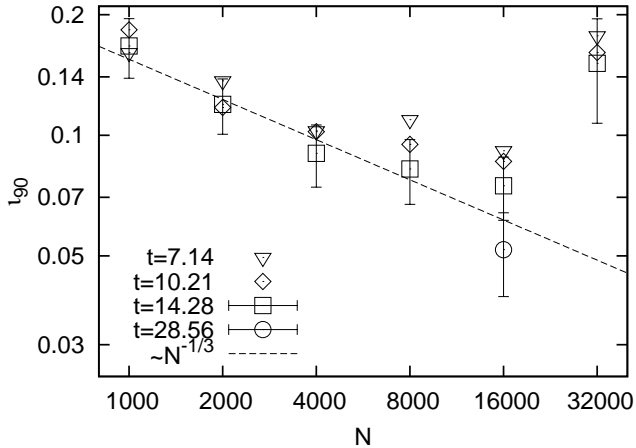


**Figure 6.** Log-log plot of ensemble-averaged  $\iota_{90}$  as a function of  $N$  measured at  $t = 7.14, 10.21$  and  $14.28 t_{dyn}$ , with a few cases extended to  $28.56 t_{dyn}$ . Dashed line corresponds to the  $N^{-1/3}$  best fit following equation (16) with data from  $N < 10000$  at  $t = 14.28 t_{dyn}$ . Error bars are calculated in the same way as in Fig. 4.

flattenings within that time, with discrepancy growing with  $N$ . These tendencies may imply that the relaxation is still undergoing and the overall agreement may possibly be improved if the simulations are extended further. To verify this, four selected cases for  $N = 16000$  are prolonged to  $28.56 t_{dyn}$ . The ensemble-averaged  $\iota_{80}$  is included in the figure with error bar corresponding to the standard deviation of the extended realizations. We find that the point passes the prediction line and stays slightly below. At this time, it is closer to the prediction than the previous snapshot.

To verify if the ensemble-averaged  $\iota_{80}$  is in coherence with the real flattening of stationary state, the superpositions of  $(\hat{e}_{zz}, \hat{e}_{xx})$  projections at  $t = 14.28 t_{dyn}$  for 80% bound particles from all realizations with  $N = 1000$  and  $8000$  are shown in Fig. 5. Projection of each realization is produced separately on to its  $(\hat{e}_{zz}, \hat{e}_{xx})$  plane before being

superposed. Ellipses in solid lines corresponding to  $\iota_{80}$  at that time are put for comparison. We find that both configurations are in good forms with the ellipses. It therefore appears that  $\iota_{80}$  is an appropriate measure to represent the flattening of the stationary state.

Then the plot of ensemble-averaged  $\iota_{90}$  as a function of  $N$  for the same time slices is shown in Fig. 6 with the  $N^{-1/3}$  best fit with points from  $N \leq 8000$  cases at  $t = 14.28 t_{dyn}$  in dashed line. The error bars are determined in the same way as described above. Comparing with the plot of  $\iota_{80}$  in Fig. 4, we find that the flattening derived from  $\iota_{90}$  is slightly greater. The overall appearance is similar and the  $N^{-1/3}$  decay is still retained. We also note the late evolution towards the prediction after the virialization for  $N = 16000$ .

From these two plots, we find an interesting remark that both  $\iota_{80}$  and  $\iota_{90}$  for  $N = 16000$  require relaxation time to prediction longer than  $14.28 t_{dyn}$ , while for smaller  $N$  they are relaxed to the prediction well before with fluctuations around the predicted stationary states observed. To inspect this evolution, the extended plots of temporal evolutions of  $\iota_{80}$  and  $\iota_{90}$  with  $N = 16000$  and  $32000$ , one realization for each  $N$ , are shown in Fig. 7. In these figures, we capture the slow decay of both  $\iota$ . For  $N = 16000$  the attainment to stationary values is observed at  $t \sim 20 t_{dyn}$ . Thus, we can safely presume the stationarity at  $t = 28.56 t_{dyn}$  for  $N = 16000$  in Figs. 4 and 6. For  $N = 32000$ , the decay lasts longer. We observe the apparent stationarity of  $\iota_{80}$  at  $t \sim 25 t_{dyn}$  but it is not clear for  $\iota_{90}$ . From these results, we verify the existence of secondary evolution that leads the virialized core to the state with lower  $\iota$ , but still non-zero. To inspect further in configuration space, the superpositions of  $(\hat{e}_{zz}, \hat{e}_{xx})$  projections for 80% bound mass with  $N = 4000$  at  $t = 3.57 t_{dyn}$  and  $14.28 t_{dyn}$  are shown in Fig. 8, with ellipses equivalent to  $\iota_{80}$  at that time as references. Note that the former is taken just after the virialization with  $\iota_{80} = 0.13$  and the latter is when the system is already in the predicted stationary state with  $\iota_{80} = 0.082$ . We find that the projected core is relaxed to elliptical form since shortly after the virialization and, following the reported  $\iota_{80}$ , it is more rounded out at the end of simulation. Further discussion

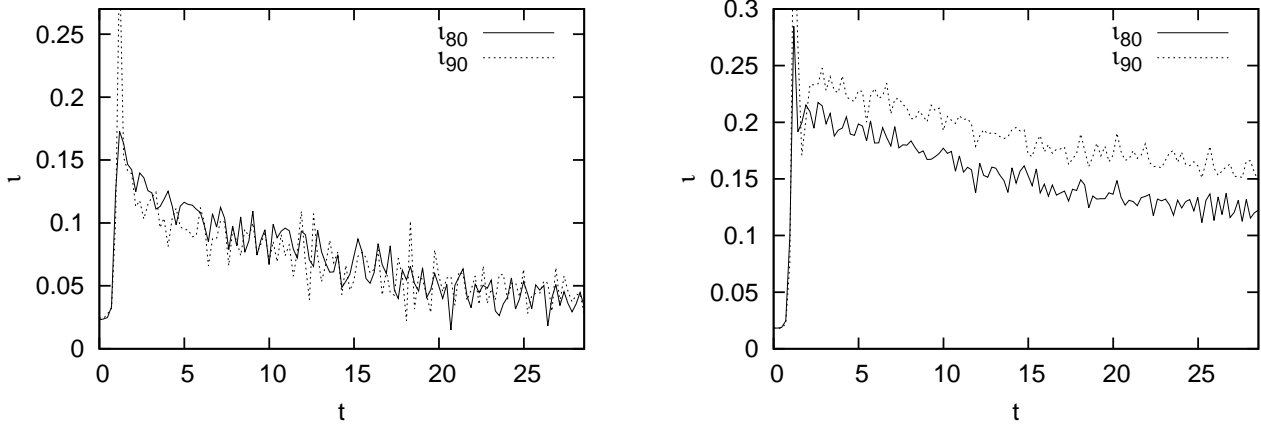


**Figure 7.** Extended temporal plots of  $l_{80}$  and  $l_{90}$  for selected realizations with  $N = 16000$  (left) and  $32000$  (right).

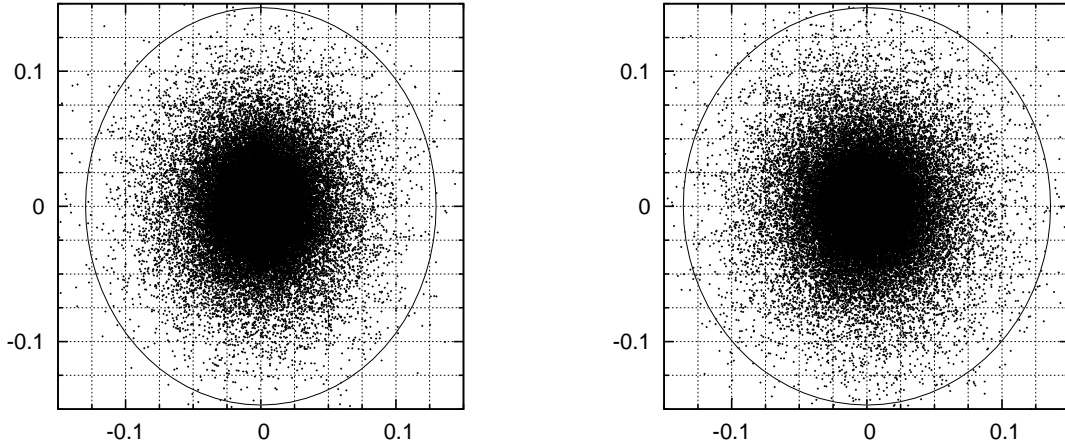


**Figure 8.** Superpositions of  $(\hat{e}_{zz}, \hat{e}_{xx})$  projections of 80% bound particles from all realizations with  $N = 4000$  at  $t = 3.57 t_{dyn}$  (left) and  $t = 14.28 t_{dyn}$  (right). The ensemble-averaged  $l_{80}$  are equal to 0.13 and 0.082, respectively. Ellipses in solid lines correspond to  $l_{80}$  at that time.

concerning these issues with reference to past study will be provided in Section 5.

Now the ensemble-averaged  $l_{100}$  as a function of  $N$  with error bars is shown in Fig. 9, along with  $N^{-1/3}$  the best fit with points at  $t = 14.28 t_{dyn}$  for comparison. We see that the plot of  $l_{100}$  is different from two previous  $l$  in many aspects. The flattening estimated from  $l_{100}$  is, as expected, significantly greater but there is relatively low dispersion of  $l_{100}$  from three time slices. The measured  $l_{100}$  clearly does not follow the  $N^{-1/3}$  prediction. The  $N$ -dependence is even absent in this plot. Unlike two previous  $l$ , it seems that extending the simulations will not change the results any further. The fact that  $l_{100}$  behaves differently from  $l_{80}$  and  $l_{90}$  could be explained by, in continuity from Section 4.1, that it is strongly correlated to the outermost halo. This part is shown to be decoupled from the core since the very beginning of the violent relaxation and makes the shape determination improper.

In summary, this section demonstrates clearly the  $N$ -dependence of the cores in the way that it tends to be more flattened out as  $N$  decreases. The relaxed cores are in good agreement with the prediction provided in Section 2.1. For

large  $N$  systems, it appears that the relaxation process is longer, which reflects the secondary evolution after the virialization. This process can be seen by the slow evolution towards more spherical, but still triaxial, configuration.

### 4.3 Variation of intrinsic three-dimensional shapes

We study in this section how the final intrinsic shapes vary in different realizations. Note that we anticipate the variation of shape because of the presence of the microscopic density fluctuation that is distributed randomly in each realization. Given a system of semi-principal axes of lengths  $a$ ,  $b$  and  $c$ , we define the triaxial indices

$$\alpha = \frac{a-b}{b} \quad \text{and} \quad \gamma = \frac{b-c}{b}. \quad (26)$$

We suppose that only four forms of ellipsoids are attainable: prolate, oblate, triaxial and spherical. Then the criterion to

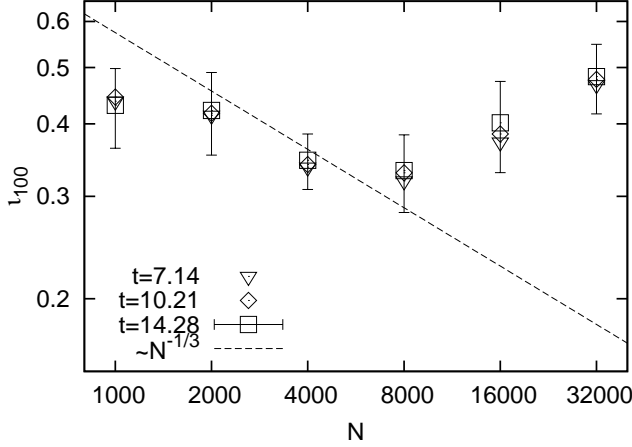


**Figure 9.** Log-log plot of ensemble-averaged  $t_{100}$  as a function of  $N$  measured at  $t = 7.14, 10.21$  and  $14.28 t_{dyn}$ . Dashed line corresponds to the  $N^{-1/3}$  best fit from equation (16) performed with data at  $t = 14.28 t_{dyn}$ . Error bars are calculated in the same way as in Fig. 4.

allocate to these four shapes is as follows:

$$\begin{aligned}
 \text{prolate} &: \alpha > \delta \quad \text{and} \quad \gamma \leq \delta \\
 \text{oblate} &: \alpha \leq \delta \quad \text{and} \quad \gamma > \delta \\
 \text{triaxial} &: \alpha > \delta \quad \text{and} \quad \gamma > \delta \\
 \text{spherical} &: \alpha \leq \delta \quad \text{and} \quad \gamma \leq \delta
 \end{aligned} \tag{27}$$

where  $\delta$  is adjustable.

The intrinsic shapes of all realizations at  $t = 14.28 t_{dyn}$  for  $N$  equal to 1000, 2000, 4000 and 8000 are summarized in  $(\alpha, \gamma)$  plots in Figs 10 and 11 for 80 and 90 per cent bound mass, respectively. In this section, the cases with  $N > 8000$  are excluded from our study as it was seen that these systems may not be fully relaxed at that time. Separating lines following the criterion (27) are drawn in dashed with  $\delta = 0.04$ . According to the plots, the intrinsic shapes of all realizations are not unique as they vary from nearly spherical, prolate, oblate to completely triaxial with various degree of triaxiality. The points from  $N = 1000$  and 2000 are spread out mostly in the prolate, oblate and triaxial regions but, when  $N$  increases, the points are less scattered and tend to gather near the origin. This result thus demonstrates once again the tendency towards spherical symmetry in system with large  $N$ .

To study this topic more quantitatively, the fractions of number of realizations in each shape as a function of  $N$  are plotted in Fig. 12 for 80 and 90 per cent bound mass, using the same  $\delta$  as in previous figures. Let us consider the  $N$ -dependence of each shape in both figures. We find that the fraction of spherical increases with  $N$ , which emphasizes the convergence towards spherical symmetry as  $N$  increases. The fraction of oblate ellipsoid also increases, on average, with  $N$  while the fraction of triaxial decreases. For the prolate, the  $N$ -dependence is not simple. It increases at first and decreases when  $N$  is greater than 4000. At  $N = 1000$ , the triaxial shape significantly dominates three others but as  $N$  increases to 8000 the oblate becomes increasingly dominant. When comparing between prolate and oblate, we find that the oblate ellipsoid is more favourable than the prolate in the range of  $N$  that we examine. The tendency to-

wards oblateness in cold initial condition was also reported by Boily & Athanassoula (2006) but the opposite result supporting the prolate was also made by Cannizzo & Hollister (1992). Thus, from those studies it appears that the conclusive answer for the preference between prolate and oblate is complicated as it correlates closely to the detail of initial density profile. However, these behaviours with  $N$  we obtained in this section may not necessarily be the same if we consider the systems with much larger  $N$ . In that limit, we expect the spherical shape to be more dominant so the fractions of three other shapes should converge down to zero.

The related work by Aguilar & Merritt (1990) also studied the similar question but, differently from us, they were focusing rather on the influence from initial parameters such as virial ratio, axial ratio or velocity anisotropy to the final shapes. It was then revealed that the final shapes depended strongly on the choice of initial parameters. Here, we investigate further the variation of final shapes when the initial condition is fixed to cold sphere of uniform density, leaving only the Poissonian density fluctuation in each realization to be varied. We find that the variation of density fluctuation, albeit in microscopic scale, can finally lead to the configurations with diverse degree of triaxiality. When  $N$  increases, the density fluctuation diminishes so the diversity of shape is less observed. Although the more precise  $N$ -dependence for each shape is not obtained in this section, the fact that the density fluctuation also takes part in establishing the final shape is crucial and not to be neglected.

#### 4.4 Specific angular momentum of ellipsoid

We present here the results about the specific angular momentum of bound structure. Let us recall that in the continuum limit the angular momentum is always absent since the motion is completely radial. While in the discrete system, the particles can have mildly orbital motion due to the local density inhomogeneity. The results in this section are arranged into two steps. First, we verify if systems possess the rotational motion after the mass ejection is finished. Secondly, if the rotation is verified, we study further how it depends on  $N$  in comparison with the estimate that we provided in Section 2.2.

Plotted in Fig. 13 are temporal evolutions of dimensionless specific angular momentum,  $j/j_0$ , computed from the 100 per cent bound mass, and three selected cases each of  $N = 1000, 2000, 4000$  and 8000 in the centre of mass frame. The characteristic specific angular momentum  $j_0$  is given by  $j_0 = r_0 v_0$ , where  $v_0 = \sqrt{\frac{GM}{r_0}}$ . In the plots, we find the similarity of evolution pattern of  $j/j_0$  in all presented cases regardless of  $N$  which can be described as follows. First it is initially zero, as it should be in cold state, and the system persists to be rotationless until approximately the first dynamical time. Then  $j/j_0$  increases sharply and relaxes shortly after, in concurrence with the virialization time. Thus from this result, we could be certain that the generation of angular momentum is initiated by the mass ejection as we suspected before. We find that the rotation is stable as, apart from the finite- $N$  fluctuation around the average,  $j/j_0$  shows no evidence of other evolution to different state. This might indicate that once the virialization is accomplished there is no further exchange of angular mo-

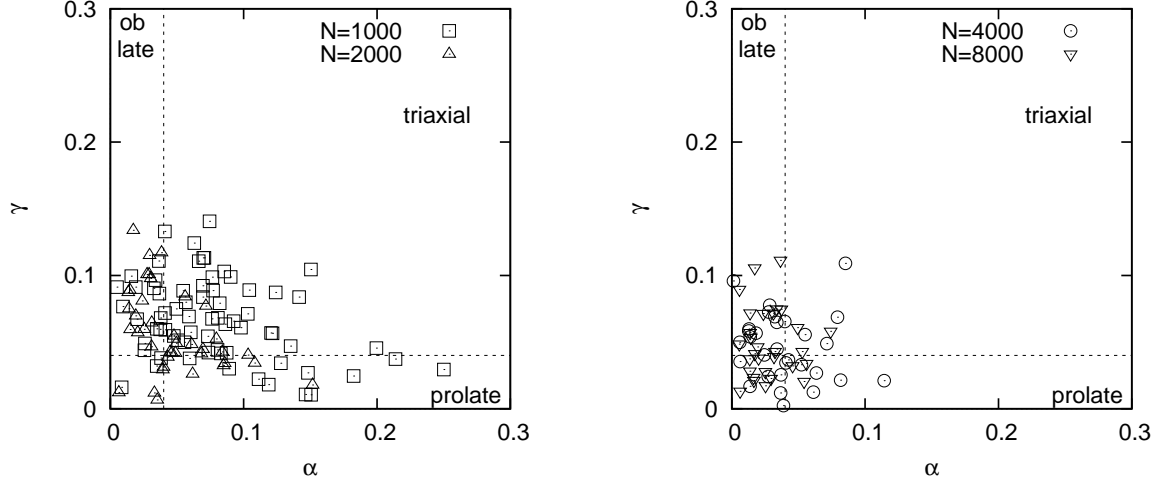


**Figure 10.** Plots of  $(\alpha, \gamma)$  from all realizations calculated from 80% bound mass for  $N = 1000, 2000$  (left), 4000 and 8000 (right) at  $t = 14.28 t_{dyn}$ . Separating lines following the criterion (27) with  $\delta = 0.04$  are put in dashed.

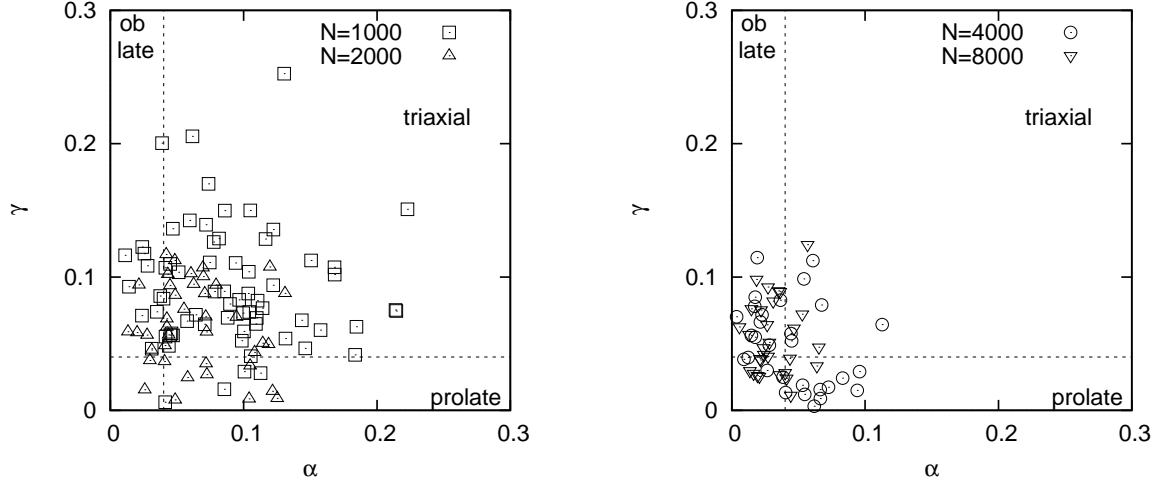


**Figure 11.** Plots of  $(\alpha, \gamma)$  from all realizations calculated from 90% bound mass for  $N = 1000, 2000$  (left), 4000 and 8000 (right) at  $t = 14.28 t_{dyn}$ . Separating lines following the criterion (27) with  $\delta = 0.04$  are put in dashed.

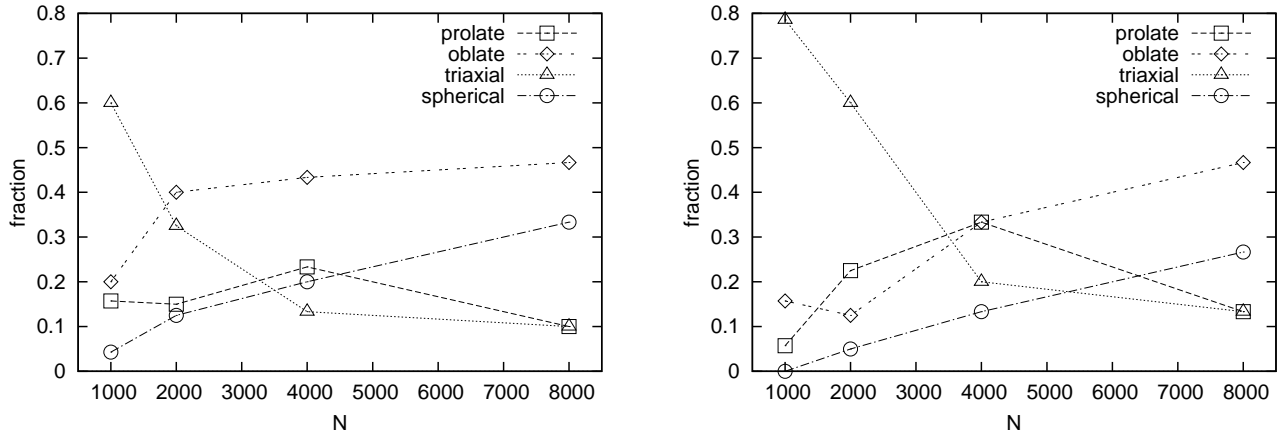


**Figure 12.** Plots of fractions of number of realizations in prolate, oblate, triaxial and spherical shapes as a function  $N$ . Left- and right-hand panels are for 80 per cent bound mass and 90 per cent bound mass, respectively.

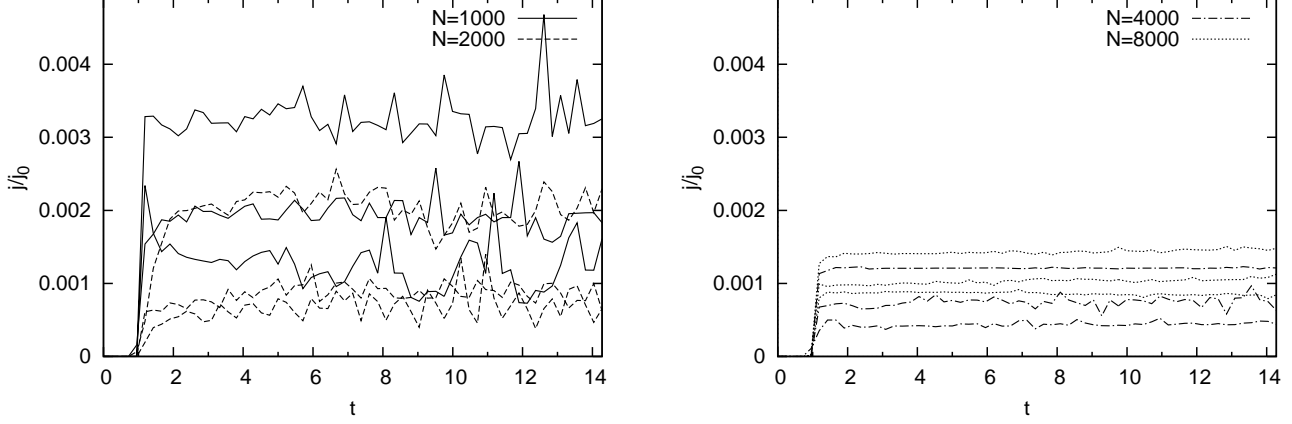


**Figure 13.** Temporal evolutions of dimensionless specific angular momentum,  $j/j_0$ , for 100 per cent bound mass with  $j_0$  given in the text. Left-hand panel is for the selected cases with  $N = 1000$  and  $2000$  while right-hand panel is for  $N = 4000$  and  $8000$ , three realizations for each  $N$ .

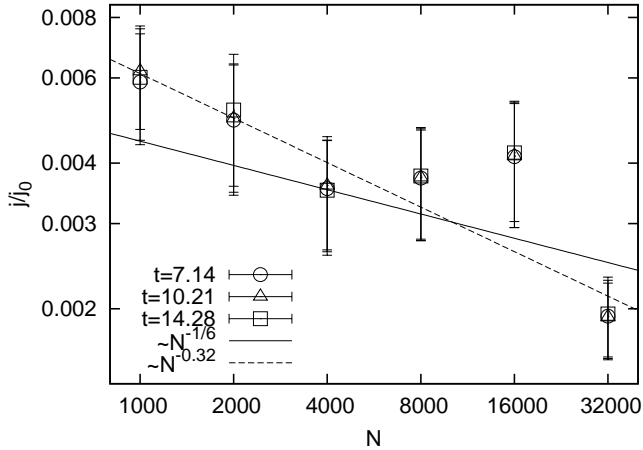


**Figure 14.** Plot of ensemble-averaged  $j/j_0$  as a function of  $N$  measured at  $t = 7.14, 10.21$  and  $14.28 t_{dyn}$ . Solid line corresponds to the  $N^{-1/6}$  best fit from equation (19) with points from three snapshots. Dashed line is the  $N^{-\lambda}$  best fit giving  $\lambda = 0.32$ . Error bars are determined in the same way as for  $\iota$  plots.

mentum between bound and ejected components. Also the angular momentum at stationary state varies considerably from realization to realization.

For more quantitative examination, the plot of ensemble-averaged  $j/j_0$  with error bars as a function of  $N$  from the 100 per cent bound mass is shown in Fig. 14, taken at the same time slices as above. Error bars are determined in the similar way as for  $\iota$  plots. The  $N^{-1/6}$  best fit from equation (19) and the  $N^{-\lambda}$  best fit giving  $\lambda = 0.32$  are provided together. In this plot, both fittings are performed with data from three time slices. We find that the dispersion of angular momentum from three snapshots is low in accordance with the temporal plot in Fig. 13. For the scaling of  $j/j_0$ , we find that the simulated  $j/j_0$  matches better with  $N^{-0.32}$ , albeit with large fluctuation, than the  $N^{-1/6}$  prediction. From this result, the  $N$ -dependence of  $j/j_0$  might reflect that the initial density fluctuation, which is the only  $N$ -dependent initial factor, is also involved in the genera-

tion of angular momentum. However, our explanation on this physical process is not yet satisfactory. The question considering the origin of angular momentum is still under investigation.

## 5 CONCLUSION AND DISCUSSION

In this paper, we study the problem of shape evolution in the  $N$ -body self-gravitating system starting from cold uniform sphere. Our main interest is on how well we can describe quantitatively the degree of deviation from spherical symmetry of the virialized structures. To begin with, we speculate that the origin of shape deformation from spherical symmetry is from the finite- $N$  density fluctuation in the way that the deformation increases with the amplitude of that fluctuation. Then by revisit of the dynamical model of spherical collapse, we implement the density fluctuation, which is purely Poissonian in our case, into the dynamical evolution and finally obtain the estimate of  $\iota$  at stationary states as a function of  $N$  to be  $N^{-1/3}$ .

In order to analyse the dynamics of shape evolution, the  $N$ -body simulations for various  $N$  have been performed. The visual inspection of the stationary state in simulation suggests that the virialized state can be described by the so-called core-halo structure, as depicted by the central dense region (or core) loosely surrounded by the diffused region (or halo). It is subsequently shown that a sub-structure consisting of 80 per cent most bound particles is acceptable to represent the core of the system and, likewise, the 90 per cent most bound mass can also be used without any significant difference. For the three-dimensional configuration of the stationary states, the temporal plots of  $\iota$  reveal the departure from spherical symmetry of the cores during the violent relaxation, and the cores in virialized state can be approximated by ellipsoids with valid three semi-principal axis lengths. Their intrinsic shapes exhibit various degrees of triaxiality and can be categorized into four different types: completely triaxial, prolate, oblate and nearly spherical. In contrast, when considering the same questions for the entire core-halo system (i.e. the 100 per cent bound mass), the

problem is less clarified as the determination of shape is erroneous due to the disturbance from distant particles in the outermost halo.

Focusing now on the  $N$ -dependence of the configurations, we find that the cores in simulations tend to be less flattened and their shapes are less diversified as  $N$  increases. We find that the predicted  $N^{-1/3}$  scaling of  $\iota$  provides reasonably good agreement with the simulated cores in the range of  $N$  from 1000 to 16000, with the extension of simulation required for  $N = 16000$ . The increase of relaxation time with  $N$  might manifest the intervention of collisional effect at this stage. This occurrence could be explained as follows. For the final state to deviate from the Vlasov limit, the scattering with the potential of neighbouring particles, which are distributed asymmetrically in microscopic scale, during close encounter is necessary. In contrast, the related study led by Roy & Perez (2004) observed the opposite results that the  $N$ -dependence was missing for the cases with  $N > 30000$  in various initial conditions. Their conclusion may be true in some part as, from our studies on various system parameters for a considerable range of  $N$ , we find that the  $N$ -dependence behaviour of each parameter differs greatly. The parameter  $\iota_{100}$  is apparently free from  $N$  while the angular momentum exposes clearly the constant decreasing with  $N$  for more than one order of magnitude (see more discussion below). For  $\iota_{80}$  and  $\iota_{90}$ , due to the increasing relaxation time with  $N$ , this question is more difficult to resolve numerically for larger  $N$ .

When we look on the temporal plots of flattenings, they reveal obviously a distinguishable process of evolution to the prediction that lasts longer than the virialization. This secondary stage leads the virialized cores to more spherical, but still triaxial, states with relaxation time diverging with  $N$ . The sequential evolutions were also reported by Theis & Spurzem (1999) where the authors demonstrated, using an appropriate measure of axial ratio, that shape evolution could be divided into three main stages: swift relaxation to triaxial configuration within a few  $t_{dyn}$ , readjustment to axisymmetric within  $\sim 20 t_{dyn}$  and slow spherization that is continual until hundreds of  $t_{dyn}$ . They asserted that the first two stages were in a collisionless regime with time-scale independent of  $N$  while only the third stage was collisional with time scale increasing with  $N$ . Back to our results, the two-step evolution scheme may coincide with their first two steps but we may have different opinions in two points. First, the underlying physical process of the second step should involve, either partly or fully, the collisionality. Thus, it appears that the collisional effect comes into regulating much earlier than previously thought by them. Secondly the shape after the second step is not necessarily axisymmetric. It was found that some final shapes ended up in triaxial. However, because of the limited simulation time in our study, we are not able to verify the third step of evolution.

Shape deformation from spherical collapse in an isolated system has also been topic of research earlier by, for example, van Albada (1982); Merritt & Aguilar (1985); Aguilar & Merritt (1990); Cannizzo & Hollister (1992); Theis & Spurzem (1999); Boily & Athanassoula (2006) for systems with  $N$  ranging from  $10^4$  to  $10^6$  with different types of initial conditions, mostly non-uniform. They found in some cases that significant triaxiality emerged even if  $N$

was as large as  $8 \times 10^5$ , while according to our conclusion the triaxiality should not remain detectable in such a system. This unlikeliness can be explained by that they employed the inhomogeneous initial density profiles that yield the density contrast which does not decay with  $N$  in addition to the Poissonian noise. Therefore, the dispersion of free-fall time is greatly enhanced even for very large  $N$  systems. Some simulations of cold collapse of power-law density profile with size comparable to our  $N = 8000$  system by Cannizzo & Hollister (1992) yielded considerably a more flattened structure. Their final axial ratio of 80% bound mass was equivalent to  $\iota$  between 0.28 and 0.44, depending strongly on the power-law index, which was more flattened than any realization in our study. However, it remains to be clarified if the same scaling is preserved for other type of initial condition. This macroscopic initial density contrast is interpreted as a ‘seed’ of instability by Roy & Perez (2004); Maréchal & Perez (2010) which is compulsory in order to develop the highly elongated structures. On the contrary, they considered the homogeneous case as lacking this seed to progress effectively the shape deformation. From our simulations, we find that the stable triaxiality still can be developed in homogeneous initial state, though it is milder than the non-homogeneous one in past studies. Thus it turns out to be that the homogeneous case may carry ‘weak seed’, which is of course of microscopic origin and decays with  $N$ , rather than ‘no seed’ as conjectured by them.

In addition, we also examine the establishment of angular momentum of stationary state starting from non-rotating cold initial condition. In past literature, the generation of angular momentum was mostly related to the tidal-torque theory (see Peebles 1969) which involved at least two systems exerting torque to each other. Here, we propose alternatively that the rotation can also be generated in an isolated system by angular momentum exchange between bound and ejected components during the asymmetric mass ejection. This supposition is verified using numerical simulations that unveil the stable rotation and the  $N$ -dependence of angular momentum at stationary states. The rotation of relaxed systems constantly slows down when  $N$  increases. We also note the short relaxation time of rotation and it is apparently independent of  $N$ . The  $N$ -dependence imprinted in the angular momentum is the crucial point which indicates that its origin is somehow related to the initial density fluctuation. However, the underlying process is not yet understood.

The author fully acknowledges the financial support granted by the Faculty of Science and Technology of the Rajamangala University of Technology Suvarnabhumi as a crucial part in conducting the research. Also useful discussions from Michael Joyce and Francesco Sylos Labini are grateful.

## REFERENCES

- Aarseth S. J., Lin D. N. C., Papaloizou J. C. B., 1988, *Astrophys. J.*, 324, 288
- Aguilar L. A., Merritt D., 1990, *Astrophys. J.*, 354, 33
- Antonov V., 1973, in Omarov G., ed., *The Dynamics of Galaxies and Star Clusters*. Nauka, Alma Ata, p. 139
- Antonov V. A., 1961, *Sov. Astron.*, 4, 859



- Barnes E. I., Lanzel P. A., Williams L. L. R., 2009, *Astrophys. J.*, 704, 372
- Barnes J., Goodman J., Hut P., 1986, *Astrophys. J.*, 300, 112
- Barnes J. E., Hernquist L., 1996, *Astrophys. J.*, 471, 115
- Binney J., 1978, *Mon. Not. R. Astr. Soc.*, 183, 501
- Boily C. M., Athanassoula E., 2006, *Mon. Not. R. Astr. Soc.*, 369, 608
- Boily C. M., Athanassoula E., Kroupa P., 2002, *Mon. Not. R. Astr. Soc.*, 332, 971
- Cannizzo J. K., Hollister T. C., 1992, *Astrophys. J.*, 400, 58
- Casertano S., Hut P., 1985, *Astrophys. J.*, 298, 80
- de Vaucouleurs G., 1953, *Mon. Not. R. Astr. Soc.*, 113, 134
- de Zeeuw P. T., 1987, in *Proc. IAU Symp. 127, Structure and Dynamics of Elliptical Galaxies*. Reidel, Dordrecht, p. 271
- de Zeeuw T., 1985, *Mon. Not. R. Astr. Soc.*, 216, 273
- Dehnen W., Gerhard O. E., 1994, *Mon. Not. R. Astr. Soc.*, 268, 1019
- Doremus J. P., Feix M. R., Baumann G., 1971, *Phys. Rev. Lett.*, 26, 725
- Hénon M., 1973, *Astron. Astrophys.*, 24, 229
- Joyce M., Marcos B., Sylos Labini F., 2009, *Mon. Not. R. Astr. Soc.*, 397, 775
- Levin Y., Pakter R., Rizzato F. B., 2008, *Phys. Rev. E*, 78, 021130
- Lynden-Bell D., 1967, *Mon. Not. R. Astr. Soc.*, 136, 101
- McGlynn T. A., 1984, *Astrophys. J.*, 281, 13
- Maréchal L., Perez J., 2010, *Mon. Not. R. Astr. Soc.*, 405, 2785
- Merritt D., Aguilar L. A., 1985, *Mon. Not. R. Astr. Soc.*, 217, 787
- Min K. W., Choi C. S., 1989, *Mon. Not. R. Astr. Soc.*, 238, 253
- Palmer P. L., Palaloizou J., 1987, *Mon. Not. R. Astr. Soc.*, 224, 1043
- Peebles P. J. E., 1969, *Astrophys. J.*, 155, 393
- Polyachenko V. L., 1981, *Sov. Astron. Lett.*, 7, 142
- Robijn F. H. A., de Zeeuw P. T., 1996, *Mon. Not. R. Astr. Soc.*, 279, 673
- Roy F., Perez J., 2004, *Mon. Not. R. Astr. Soc.*, 348, 62
- Schwarzschild M., 1979, *Astrophys. J.*, 232, 236
- Schwarzschild M., 1982, *Astrophys. J.*, 263, 599
- Springel V., 2005, *Mon. Not. R. Astr. Soc.*, 364, 1105
- Springel V., Yoshida N., White S. D. M., 2001, *New Astron.*, 6, 79
- Sylos Labini F., 2012, *Mon. Not. R. Astr. Soc.*, 423, 1610
- Sylos Labini F., 2013, *Mon. Not. R. Astr. Soc.*, 429, 679
- Theis C., Spurzem R., 1999, *Astron. Astrophys.*, 341, 361
- Toomre A., 1977, in *Tinsley B. M., Larson R.B., eds, Evolution of Galaxies and Stellar Populations*. Yale University Observatory, New Haven, p. 401
- Toomre A., Toomre J., 1972, *Astrophys. J.*, 178, 623
- van Albada T. S., 1982, *Mon. Not. R. Astr. Soc.*, 201, 939